5-2022

Multi-decadal analysis of remotely sensed vegetation change in Berea College Forest - seasonality of forest patterns using remote sensing.

Jacob Foushee
University of Louisville

Multi-decadal analysis of remotely sensed vegetation change in Berea College Forest - seasonality of forest patterns using remote sensing

By

Jacob Foushee

Submitted in partial fulfillment of the requirements

for Graduation *summa cum laude*

and

for Graduation with Honors from the Department of Geography

University of Louisville

May 2022

ACKNOWLEDGMENTS

This research could not have been accomplished without the help of Dr. Andrea Gaughan and Dr. Forrest Stevens. Their patience and instruction gave me the resources I needed to complete this research. Thank you both for your guidance. Additionally, thank you to Dr. Cynthia Corbitt for sitting on my defense committee.

TABLE OF CONTENTS

LIST OF FIGURES

LIST OF TABLES

ABSTRACT

Satellite imagery is a practical and valuable tool for monitoring vegetation condition in forests. The longevity of the USGS/NASA Landsat program along with its medium spatial resolution (30m) gives researchers the ability to make informed statements on land cover generally, and specifically on aspects such as forest conditions. The Landsat program's nearly 50-year archive of imagery show how Earth's surface has changed through modern development and how these developments have influenced forests. Google Earth Engine (GEE) is a cloud-based repository of satellite imagery dating as far back as the 1970s. This study utilizes Landsat 5-8 imagery from GEE to calculate the long-term vegetation structure trends in Berea College Forest (BCF) in Berea, Kentucky from 1984-2020. By calculating the average growing-season Normalized Difference Vegetation Index (NDVI) and using the Mann-Kendall trend test and Sen's slope estimator, I evaluated the significance of vegetation productivity trends on a pixel-by-pixel basis. The results show that 68.47% of BCF displayed significant trends in NDVI, with most of these pixels associated with a positive trend, and NDVI values for the study area increased at a rate of 0.001985 units per year. These positive trends were mostly clustered in the northern head and eastern tail of BCF. The southern portion displayed a clustering of pixels with no significant trend. Significant negative trends were rare but present. The most noticeable negative trend is attributed to US Highway 421, which began construction in 1998. Understanding long-term vegetation dynamics in BCF will assist foresters in developing effective management plans.

Keywords: forest trend analysis; google earth engine; landsat; ndvi; satellite imagery

LAY SUMMARY

Satellite imagery is a practical and valuable tool for monitoring vegetation condition in forests. The longevity of the USGS/NASA Landsat program along with its ability to resolve sub-hectare plots of land in a single pixel help researchers make informed statements on land cover generally, and specifically on aspects such as forest conditions. The Landsat program's nearly 50-year archive of imagery shows how Earth's surface has changed through modern development and how these developments have influenced forests. Google Earth Engine (GEE) is a cloud-based repository of satellite imagery dating as far back as the 1970s. This study utilizes Landsat 5-8 imagery from GEE to calculate the long-term vegetation structure trends in Berea College Forest (BCF) in Berea, Kentucky from 1984-2020. By calculating the average growing-season Normalized Difference Vegetation Index (NDVI), a proxy for photosynthetic activity, and using the Mann-Kendall trend test and Sen's slope estimator, I evaluated the significance of vegetation productivity trends on a pixel-by-pixel basis. The results show that 68.47% of BCF displayed significant trends in NDVI, with most of these pixels associated with a positive trend, and NDVI values for the study area increased at a rate of 0.001985 units per year. These positive trends were mostly clustered in the northern head and eastern tail of BCF. The southern portion displayed a clustering of pixels with no significant trend. Significant negative trends were rare but present. The most noticeable negative trend is attributed to US Highway 421, which began construction in 1998. Understanding long-term vegetation dynamics in BCF will assist foresters in developing effective management plans.

INTRODUCTION

Satellite systems can "see" beyond the visible portion of the electromagnetic spectrum, and this can be leveraged to monitor vegetation condition over large areas with the use of near-infrared light (Pelkey, Stoner, and Caro 2000). Additionally, continual, high-quality satellite imagery has been collected since the 1980s. The temporal nature of earth observation allows humanity to study the influence of development on the natural world over decades. Through satellite imagery, researchers can analyze a wide range of phenomena, making remote sensing a robust and effective tool in forest management.

The longevity of satellite programs, like the NASA/USGS Landsat program (1972-present), provides researchers with the ability to track long-term trends in forest phenology (Forkel et al. 2013; Zhu et al. 2016), and these trends portray how normal seasonal fluctuations are changing due to rising global temperatures.

The Department of Forestry at Berea College has grown and managed the Berea College Forest (BCF) -- a semi-deciduous, temperate forest -- since the late 19th century, and the department is known for testing new management techniques to better care for its forest (Perry and Patterson 2000). A compliment to those efforts is the use of remote sensing tools. Vegetation indices, like the Normalized Difference Vegetation Index (NDVI) ($NDVI = \frac{NIR-Red}{NIR+Red}$), are useful tools in analyzing phenological changes in an area (Eastman et al. 2013; Zhu et al. 2016). These indices estimate vegetation productivity by measuring the amount of near-infrared (NIR) energy reflected from the plants. Chlorophyll in plants absorbs most visible light (notably red light 630-680nm) while the cell structure of leaves reflects high amounts of NIR energy (845-885nm) (Brecht 2018). Hence, the more leaves a healthy plant has, the more these two portions of the electromagnetic spectrum are affected (Knipling 1970).

NDVI seeks to compare the difference between NIR to red energy (Liu and Huete 1995). The greater the difference between NIR and red light, the higher the NDVI score. The NDVI score is a unitless value. On a larger scale, NDVI is a proxy for the productivity of entire forests, and denser vegetation will generally lead to greater NDVI values (Naif et al. 2020). NDVI interpreted on a pixel-by-pixel basis can evaluate the variation in vegetation conditions within the forest (Piao et al. 2019). However, Landsat's 30m spatial resolution is not fine enough to capture the structure of every tree in a forest. Pixels are assigned the average digital number value found in the 30m-by-30m area. A pixel exhibiting a high NDVI value does not mean that every tree in the pixel's area will have a high NDVI value as well. While medium-resolution satellites cannot collect all the nuance in vegetation production, they are useful in analyzing large study areas, like BCF, because they have a long repository of imagery and are easily accessible (Earth Observation System 2019).

Plant phenology refers to the timing of seasonal plant advancement, like green-up and senescence. According to previous research, temperature is the driving factor in plant phenology (Vitasse et al. 2011; Chuine, Cour, and Rousseau 1999). Continued research into phenological shifts in local forests is important as the timing of plant cycles is extremely sensitive to changes in the climate system (Piao et al. 2019). The growing season in Berea typically ranges from mid-April to mid-October (USDA 2012). For this research, I will define the growing season as beginning on April 15th and ending on October 15th.

The impact of climate change on a forest's seasonal dynamics varies from region to region (Melaas, Sulla-Menashe, and Friedl 2018), but studies highlight that the trends in temperate forests show earlier green-up (Melaas, Sulla-Menashe, and Friedl 2018; Piao et al. 2019; Vitasse et al. 2011). Multiple studies have identified an earlier start to the growing season with a shift in

timing for temperate forests (Piao et al. 2019; Vitasse et al. 2011; Linderholm 2006), correlating with an expected increase in NDVI values during the growing season.

GEE is a freely available software that does not require users to download large datasets (Chen et al., 2021). GEE is flexible in that users can developed their own scripts to answer questions specific to their interests, such as monitoring forest structure or tracking land cover over time. Furthermore, GEE can be applied to any region of the world to observe a wide range of land cover types, including temperate forests and savannas (Alencar et al., 2020; Schmid, 2017). The platform maintains entire series of satellite imagery that can be quickly accessed, analyzed, and processed in the cloud. Since users can easily access whole satellite series, multi-decadal trend analysis is a common application of GEE (Alencar et al., 2020; Chen et al., 2021; Schmid, 2017). Since forests are critical to the global climate, GEE is frequently used to monitor long-term trends in forest condition (Brovelli et al., 2020; Sankey et al., 2020).

Two statistical tests commonly used in analyzing biophysical data are the Mann-Kendall Trend Test and Sen's Slope Estimator (Douglas, Vogel, and Kroll 2000; Tabari and Marofi 2010; Gocic and Trajkovic 2013). The article by Gocic and Trajkovic demonstrates the utility of these statistical tests. The authors tested the significance of weather data in Serbia and identified significant positive trends in maximum and minimum temperatures, among other factors. These tests evaluate remotely sensed trends in long-term vegetation patterns. In this research, I will be conducting trend analyses of NDVI calculated on composited median reflectance images in the red and NIR bands across the growing season.

The objective of this research is to evaluate NDVI trends in BCF during the growing season. The central question framing this research is - *has the growing season NDVI in BCF shifted since 1984*? I hypothesize that growing season NDVI in BCF will trend larger during the

study period, meaning vegetation production is increasing. If true, BCF will need to develop management techniques that are adapted to the longer growing season and are flexible to future changes in the local climate.

Significance

Extensive research on phenological changes due to climate change shows that spring is beginning earlier in temperate forests across the planet (Melaas, Sulla-Menashe, and Friedl 2018; Piao et al. 2019; Vitasse et al. 2011; Linderholm 2006; Menzel 2000). However, the magnitude of change varies from place to place (Melaas, Sulla-Menashe, and Friedl 2018). This research is significant in understanding the nuance of phenological timing in a small forest.

Study Area

The study area is Berea College Forest (BCF) (Figure 1). BCF is a temperate, semi-deciduous forest located adjacent to Berea College. The College has often used the forest to test innovative forest management techniques, the most recent being prescribed burning which started in 2019. BCF is certified by the Forest Stewardship Council and has goals to sequester carbon, provide recreational activities, improve the water supply to Berea, and grow lumber sustainably.

BCF has grown considerably during its lifetime. The college began purchasing land in 1898 with the expressed purpose of pioneering forestry in the US, a primarily European discipline until this point (Perry and Patterson 2000). Much of the land was in poor condition when it was acquired. Agriculture was the dominate force in the area that clear cut broad swaths of the land. Over farming and over grazing had severely degraded the soil quality. As Berea College slowly amassed land, the lead foresters implemented new management techniques, like seedling nurseries and tree thinning, to support native species. Today, the forest spans over 9,000

acres and serves as a demonstration of adaptive forest management in the Appalachian region. Furthermore, the forest is home to over 12 miles of trails, and the Department of Forestry is committed to teaching users how to best take care of their forest.

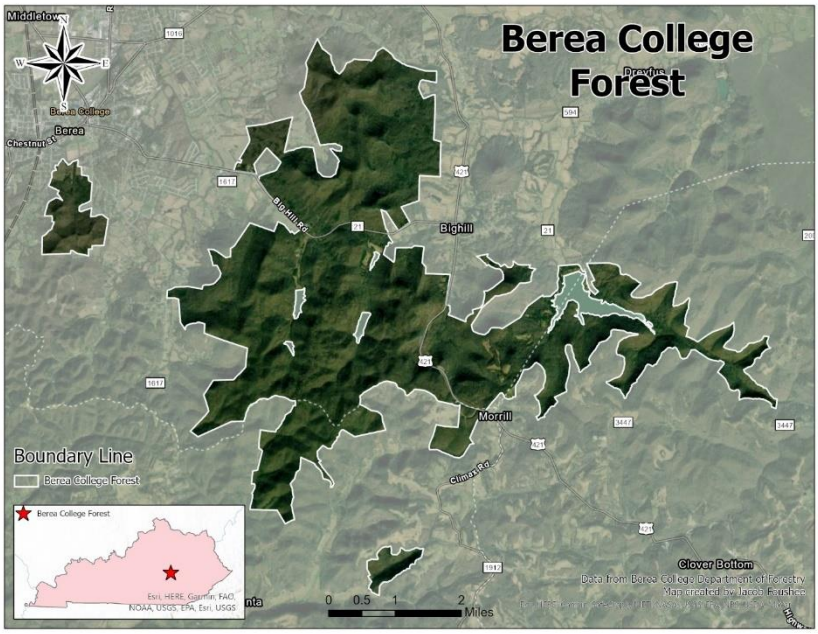

Figure 1. *Map showing the extent of Berea College Forest*

This research is complimentary to another undergraduate thesis (Hinzee Smith, 2022) and her inquiry into the perception of prescribed burns in BCF. To evaluate public perception, Hinzee sent short questionnaires to landowners living near the forest. If recipients show further interest, Hinzee conducted interviews to elaborate on any questions asked in the survey along with any other information the interviewee decides to mention. Public perception of forest management techniques is closely tied to vegetation productivity.

DATA AND METHODS

Data

This study leverages Landsat imagery from Google Earth Engine (GEE) beginning in 1984. The Landsat mission is the longest running satellite series, collecting data as far back as

1972. Since this study begins analysis in 1984, I used imagery from Landsat 5 through Landsat 8 (Table 1; Table 2). The image collections used in the study were USGS Landsat 5 Level 2, Collection 2, Tier 1; USGS Landsat 7 Level 2, Collection 2, Tier 1; and USGS Landsat 8 Level 2, Collection 2, Tier 1. Each of the datasets contained atmospherically corrected land surface reflectance values from their respective satellites. Due to the 2003 scan line corrector error in Landsat 7, this study used Landsat 7 imagery only when necessary. The data were filtered by date. Landsat 5 imagery was used from 1/1/1984 – 12/31/2011, Landsat 7 imagery was used from 1/1/2012 – 12/31/2013, and Landsat 8 imagery was used from 1/1/2014 – 12/31/2020.

	Spatial Resolution (m)	**Years Active**	**Return Time (days)**	**Radiometric Resolution (bits)**
Landsat 5	30	1984-2013	16	8
Landsat 7	30	1999-present*	16	8
Landsat 8	30	2013-Present	16	12

Table 1. *Spatial, temporal, and radiometric resolutions of Landsats 5, 7, & 8 (USGS 2021a)*

**Scan Line Corrector Malfunction in 2003*

In addition to the Landsat imagery, I imported a shapefile of BCF from the Berea College Department of Forestry to overlay the GEE outputs. The area of analysis was a polygon that encompassed BCF. The coordinates of the polygon are [-84.311, 37.485], [-84.132, 37.485], [-84.132, 37.591], and [-84.311, 37.591]. I included this polygon to provide a broader picture of vegetation structure around BCF.

	Landsat 5	Landsat 7	Landsat 8
Bands 3	Red 630-690nm	Red 630-690nm	-
Band 4	NIR 770-900nm	NIR 770-900nm	Red 640-670nm
Band 5	-	-	NIR 850-880nm

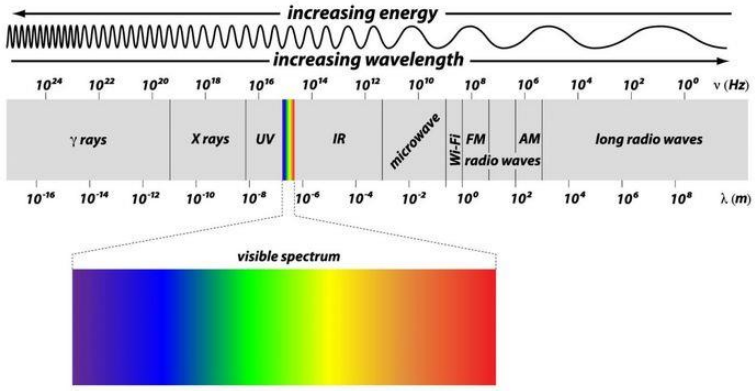

Table 2. *Spectral bands of Landsats 5, 7, & 8 and the electromagnetic spectrum (FComm 2020)*

I collected an image of growing season NDVI values for each year beginning in 1984 and continuing to 2020 by pulling out median pixel values from all images collected during the growing season and producing a composited image. The images covered BCF and portions of the surrounding area. These data were freely accessible.

Methods

To analyze the data, I used Google Earth Engine (GEE), a cloud-based computing tool, to calculate the trend of Landsat-derived NDVI in BCF from 1984 to 2020. Specifically, I calculated the growing season NDVI (April-October) on the median composited image on pixel-by-pixel basis for the study area. My source code is in Appendix 1.

After importing the previously mentioned image collections and filtering the collections by date, I merged the three datasets into one aggregate image collection. These merged data were the basis for analysis in GEE.

I first calculated a composite image for each year in the study period. To do this, I created a function to pull out the median digital number value of every pixel from images collected for one year. Extracting the median pixel value removes the influence of extreme values, like clouds, that would otherwise distort the imagery if the data were composited with mean pixel values. With the median values, I created a composite image that represented the year. This process was repeated for every year in the study period.

I then created a time stamp function to arrange the composited images temporally. This was done to order the composited images so the program could appropriately evaluate the long-term NDVI trends. Next, I calculated NDVI for each of the composited images in the study period.

Mann-Kendall Trend Test

The Mann-Kendall is a nonparametric, ranked-based statistical test useful for evaluating trends in time series. The data points are ranked in order by date. Each data point is then compared to all following data points, creating image pairs. The test is looking for differences in relative magnitude of one data point to all following data points. If the magnitude of data points changes over time, then a trend is present (Douglas, Vogel, and Kroll 2000; Tabari and Marofi 2010). The trend test is characterized as the sum of the signs of all image pairs. The Mann-Kendall is used for identifying whether a pixel is statistically significant or not, but this test does not indicate the magnitude of significance.

The Mann-Kendall trend test *S* statistic is calculated as

$$S = \sum_{i=1}^{n-1} \sum_{j=i+1}^{n} sgn(x_j - x_i) \qquad (1)$$

where n is the total number of data points, x_i and x_j are the data values in time series i and j when $j > i$. The sgn(x_j - x_i) is written as

$$\text{sgn}(x_j - x_i) = \begin{cases} +1, \text{if } x_j - x_i > 0 \\ 0, \text{ if } x_j - x_i = 0 \\ -1, \text{if } x_j - x_i < 0 \end{cases} \quad (2)$$

Variance for the data is then calculated, and a Z-score is determined. Positive Z-scores indicate an upward NDVI trend, negative Z-scores show a downward NDVI trend, and a Z-score of 0 means there is no significant trend in NDVI values since the 1980s (Gocic and Trajkovic 2013).

To calculate the Mann-Kendall trend test in GEE, I imported code from the GEE tutorial site. This piece of code iterates over each pixel of the collection and calculates the trend sign of the pixel compared to each of the pixels that follow the original chronologically. The output of this is an image indicating the distribution of pixels with significant positive or negative NDVI trends along with pixels showing no significant change.

Sen's Slope Estimator

Sen's Slope Estimator is a nonparametric statistical test that builds on the Mann-Kendall trend test. This test calculates the slope of a linear trend in a time series by finding the median of the slopes of all lines through a pair of data points. Sen's slope shows the magnitude and slope of the trend calculated from the Mann-Kendall trend test. This test is useful because it is not influenced by outliers (Tabari and Marofi 2010; Gocic and Trajkovic 2013). In the case of my research, Sen's slope estimator runs through the image pairs and identifies the magnitude of difference in NDVI between each of the pairs on a pixel-by-pixel basis.

The Sen's Slope Estimator is calculated as

$$Q_i = \frac{x_j - x_k}{j-k} \text{ for } i = 1, \ldots, N \quad (3)$$

where x_j and x_k are the values at times j and k where $j > k$. The values for Q_i for each pixel are then ranked in ascending order, and the median of the slope is determined by

$$Q_{med} = \begin{cases} Q\left[\frac{N+1}{2}\right] & \text{if } N \text{ is odd} \\ \frac{Q_{\left[\frac{N}{2}\right]} + Q_{\left[\frac{N+2}{2}\right]}}{2} & \text{if } N \text{ is even} \end{cases} \quad (4).$$

The sign of Q_{med} denotes the direction of the trend while that value shows the steepness of the trend (Gocic and Trajkovic 2013).

To determine Sen's slope and intercept for BCF, I pulled code from the GEE tutorial website. Sen's slope works similarly to the Mann-Kendall, but it instead focuses on the values calculated for the image pairs. This statistical test selects the median slope computed from all image pairs. This test is evaluated on a pixel-by-pixel basis. Red pixels indicate a decreasing trend in vegetation condition while green pixels represent an increasing trend.

Significance Test

After running the Mann-Kendall trend test and Sen's slope estimator, I created a binary classification of significant trends in NDVI on a pixel-by-pixel basis. I pulled this code from the GEE tutorial website. Through this code, I calculated the z-statistic for each statistic based off the variance output from the Mann-Kendall trend test. I then conducted a two-sided p-value test at the 95% confidence interval to draw out the pixels with significant increasing and decreasing trends in NDVI.

RESULTS

The output of my analysis shows that there is a slight positive increase of growing season NDVI in BCF between 1984-2020 (Table 3; Table 4). The trendline denotes an increase in NDVI at a rate of 0.001985 units per year. The graph shows dips in NDVI in 1985, 1991, 1993, and 2002. These are the only years when growing season NDVI values go below 0.300. Prior to 2000, NDVI values did not go beyond 0.400. However, eight out of the 20 years following 2000 exhibited NDVI values above 0.400, and the years 2014-2018 all showed values greater than 0.400.

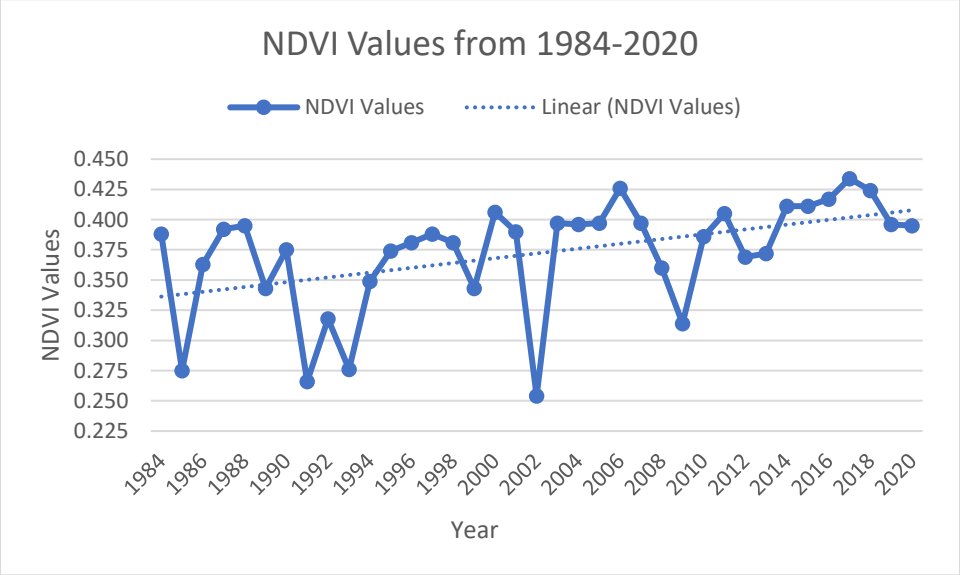

Table 3. *Line chart of growing season NDVI values from 1984-2020 in BCF*

Year	*NDVI Values*
1984	0.388
1985	0.275
1986	0.363
1987	0.392
1988	0.395
1989	0.343
1990	0.375
1991	0.266
1992	0.318
1993	0.276
1994	0.349
1995	0.374
1996	0.381
1997	0.388
1998	0.381
1999	0.343
2000	0.406
2001	0.39
2002	0.254
2003	0.397
2004	0.396
2005	0.397
2006	0.426
2007	0.397
2008	0.36
2009	0.314
2010	0.386
2011	0.405
2012	0.369
2013	0.372
2014	0.411
2015	0.411
2016	0.417
2017	0.434
2018	0.424
2019	0.396
2020	0.395

Table 4. *Growing season NDVI values from 1984-2020 in BCF*

The results of my analysis show that 68.47% of BCF exhibits a significant trend in NDVI since 1984, and most of these pixels display a significant positive trend as shown in Figure 2. Figure 2 shows the results of the Mann-Kendall trend test. The cross-hatching indicates significant trends. Green pixels represent positive trends, yellow pixels exhibit no trend, and red pixels indicate negative trends. While positive trends were more common, negative significant trends are, on average, stronger than the positive trends.

The data show a clustering of trends in BCF. Based on Figure 2, significant positive NDVI trends appear most commonly in the northern head of the main body of the forest while the southwestern portion shows a mixture of significant positive trends with no significant trend. In the center of BCF is a line showing a significant negative trend. This object denotes US Highway 421, which began construction in 1998. The eastern tail of BCF is mostly made of pixels with a positive significant trend while there are pixels with no trend along the southern

rim.

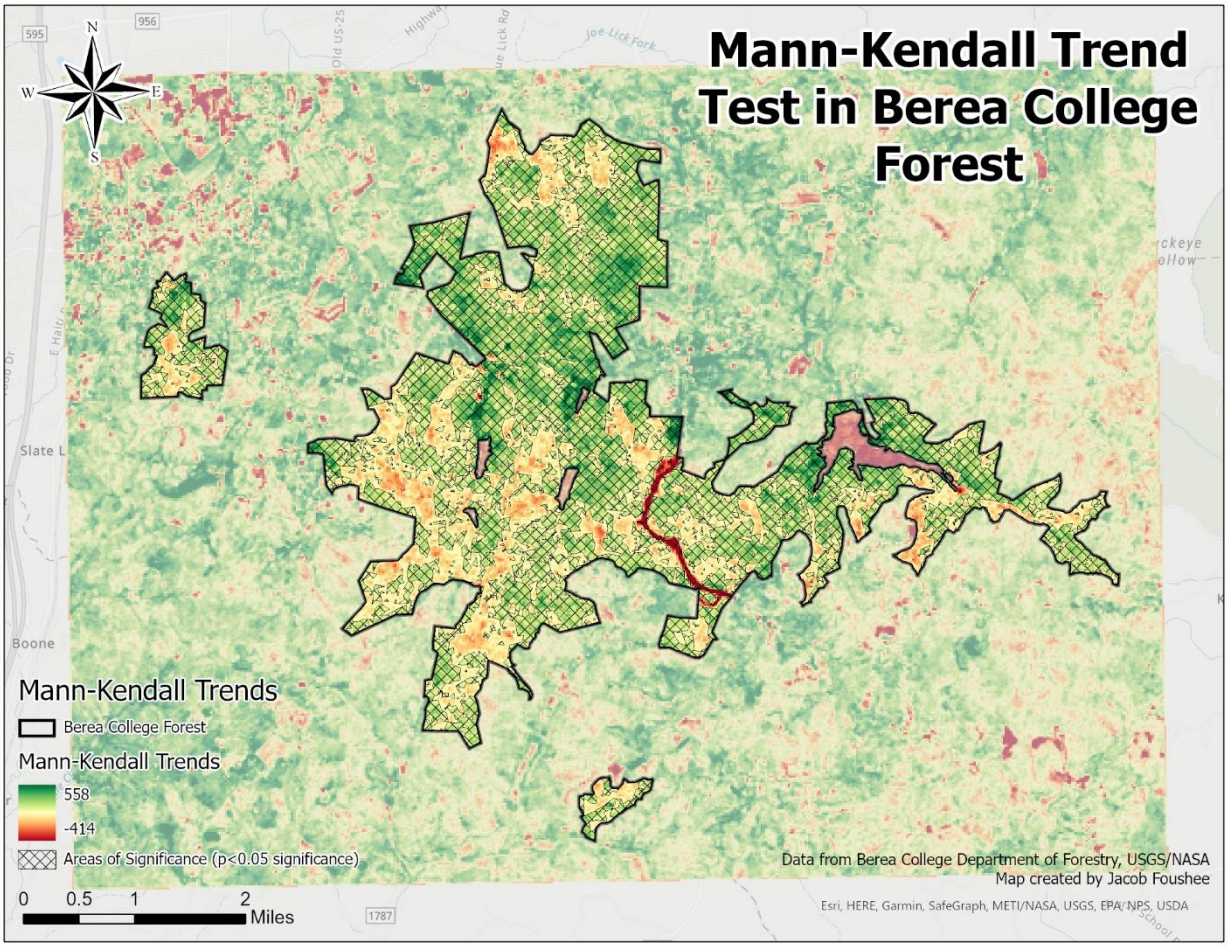

Figure 2. *Mann-Kendall Trend Test in BCF*

The Sen's slope estimator output from GEE displays the median slope of the trends evaluated through the Mann-Kendall trend test (Figure 3). The region attracting the most attention in Figure 3 is US Highway 421. This road shows a significant negative trend in annual NDVI. Table 5 provides an example of NDVI values of one pixel located along US Highway 421. Construction for the highway began in 1998. NDVI values along the highway plunge from 1997 to 1998. Following construction, NDVI values averaged to half of what they were prior to 1998. The Sen's slope value associated with this pixel amounted to a declining slope of -0.0000192 NDVI units per year. Pixels showing a positive significant trend generate a positive

Sen's slope value, but the rate at which these NDVI values are increasing has a smaller magnitude than pixels located along the highway.

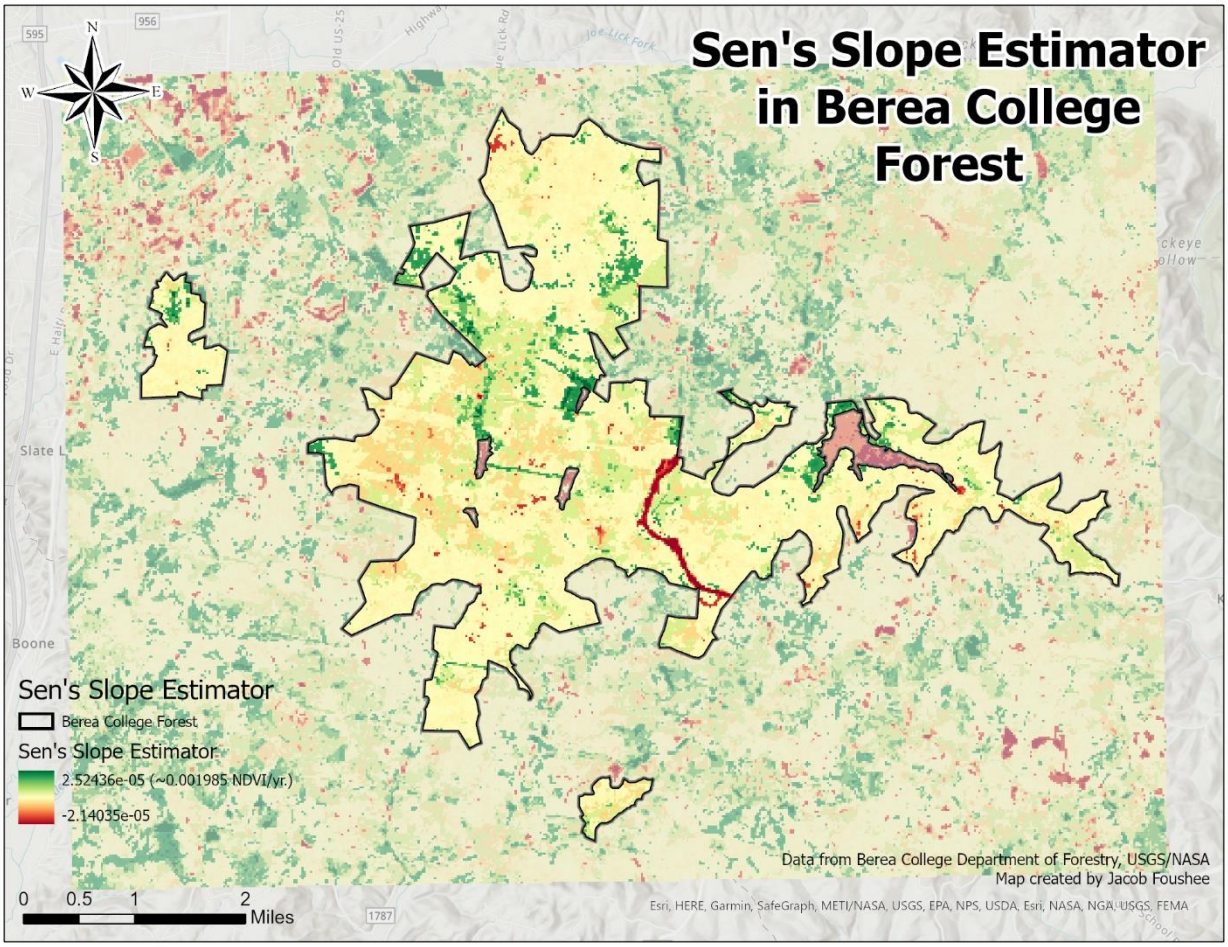

Figure 3. *Sen's Slope Estimator in BCF*

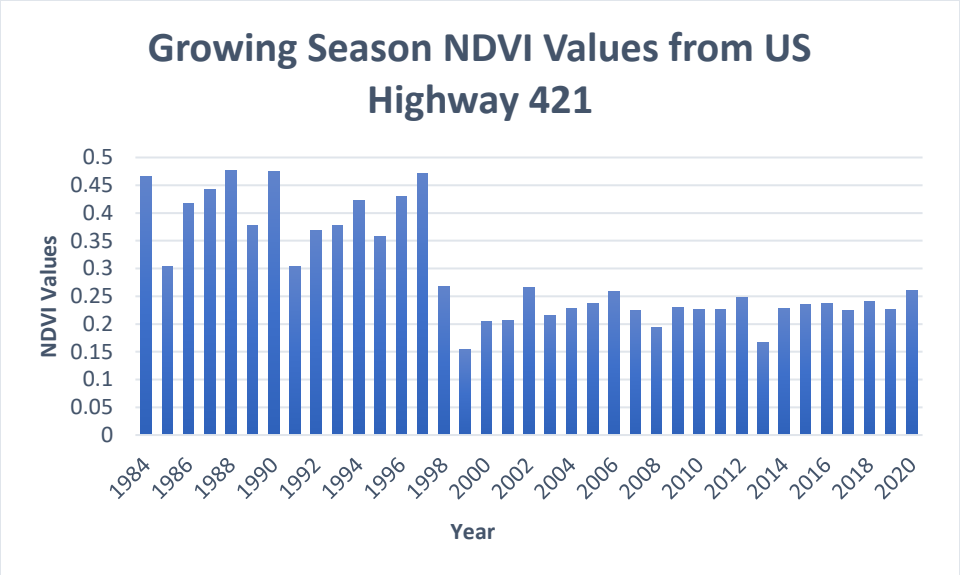

Table 5. *Growing season NDVI values from Highway 421*

DISCUSSION

The results of my study indicate that 68.47% of the study area displayed significant trends in growing season NDVI between 1984-2020. Many of these trends were positive. However, the rate at which average NDVI values increased over the study period was slight, approximating to an increase of 0.001985 units per year. Furthermore, areas with significant trends appeared to be clustered. Significant positive trends took place in the northern head and eastern tail of BCF. Significant negative trends were present but were concentrated to a line bisecting BCF. These trends denoted US Highway 421, which began construction in 1998. Finally, areas exhibiting no significant trends were clustered in the southwestern portion of the forest and along the southeastern forest edge.

The results of this study fail to reject the hypothesis that growing season NDVI would increase in BCF from 1984-2020. While the rate of growth is less than expected, vegetation production, as noted by the NDVI signal, has been increasing over time in BCF. These results

could point to a possible expansion in the growing season, but further research into start of season and end of season timing in BCF is needed. The historical growing season in BCF ranges from mid-April to mid-October. In this study, I defined the growing season to begin on April 15th and end on October 15th. Since warmer temperatures and increased precipitation will likely lead to the growing season beginning earlier than April 15th in BCF, vegetation will have begun development before the normal growing season. Moreover, warmer temperatures will extend the growing season beyond October 15th, meaning the end of season will be delayed (Dragoni and Rahman 2012). These two implications lead to mature plants reflecting more NIR energy at the beginning and end of the historical growing season. In terms of remote sensing, NDVI values at the beginning and end of the normal growing season will trend larger over time.

These results also emphasize the difference in impact of direct and indirect human land cover change. Most significant negative trends in the study area are attributed to US Highway 421, which began construction in 1998. Rapid land cover change in the area led to a sharp decline in NDVI values in 1998, and values remained relatively low for all following years. However, most pixels exhibited a slight significant positive trend that cannot be directly tied to a change in vegetation type or human-induce land cover change.

Further analysis would seek to correlate the results found in this study with factors critical to plant growth, like precipitation and temperature. Examining long-term trends in these phenomena would build on this research by further demonstrating changes in the climate of the region. The Sixth Assessment Report from the Intergovernmental Panel on Climate Change (IPCC) states that regional average temperatures along with extreme temperatures are virtually certain to rise (Arias et al., 2021). Additionally, the authors predict that mean and extreme precipitation are very likely to increase. Figure 4 shows the distribution of projected temperature

and precipitation change during the 21st century according to two different climate scenarios. The RCP 8.5 scenario shows predictions for a future where nations do not take significant action in reducing emissions while the RCP 2.6 scenario is a low emission. As predicted by RCP 8.5, climate change will likely lead to hotter temperatures and greater precipitation in the eastern United States. According to the Seasonality and Climate Change report from the EPA, average surface temperatures across the contiguous US have increased at a rate of 0.16°F per decade since 1901, and summers have become 1°F hotter in most of the southeastern US (EPA, 2021). Contrary to the IPCC predictions, the EPA report found that precipitation decreased between 1901-2015 in the southeastern US.

Temperature is the driving factor in plant phenology (Vitasse et al. 2011; Chuine, Cour, and Rousseau 1999), and precipitation plays an important role in plant development. These two components also indirectly influence other variables critical to plant development, like soil moisture. Research into the relationship between increasing temperature and precipitation on vegetation structure would further our understanding of climate change in BCF. Identifying the beginning and end of the growing season from 1984 to the present would provide deeper insight into how the growing season's timing is shifting. Furthermore, climate change is influencing the frequency and severity of seasonal extremes, like heatwaves and forest fires, along with expanding the time of the year they occur (EPA 2021). A stronger understanding of these factors in BCF will help foresters develop management techniques that can compensate for future climatic changes, such as adjusting drainage patterns to account for more extreme storm events.

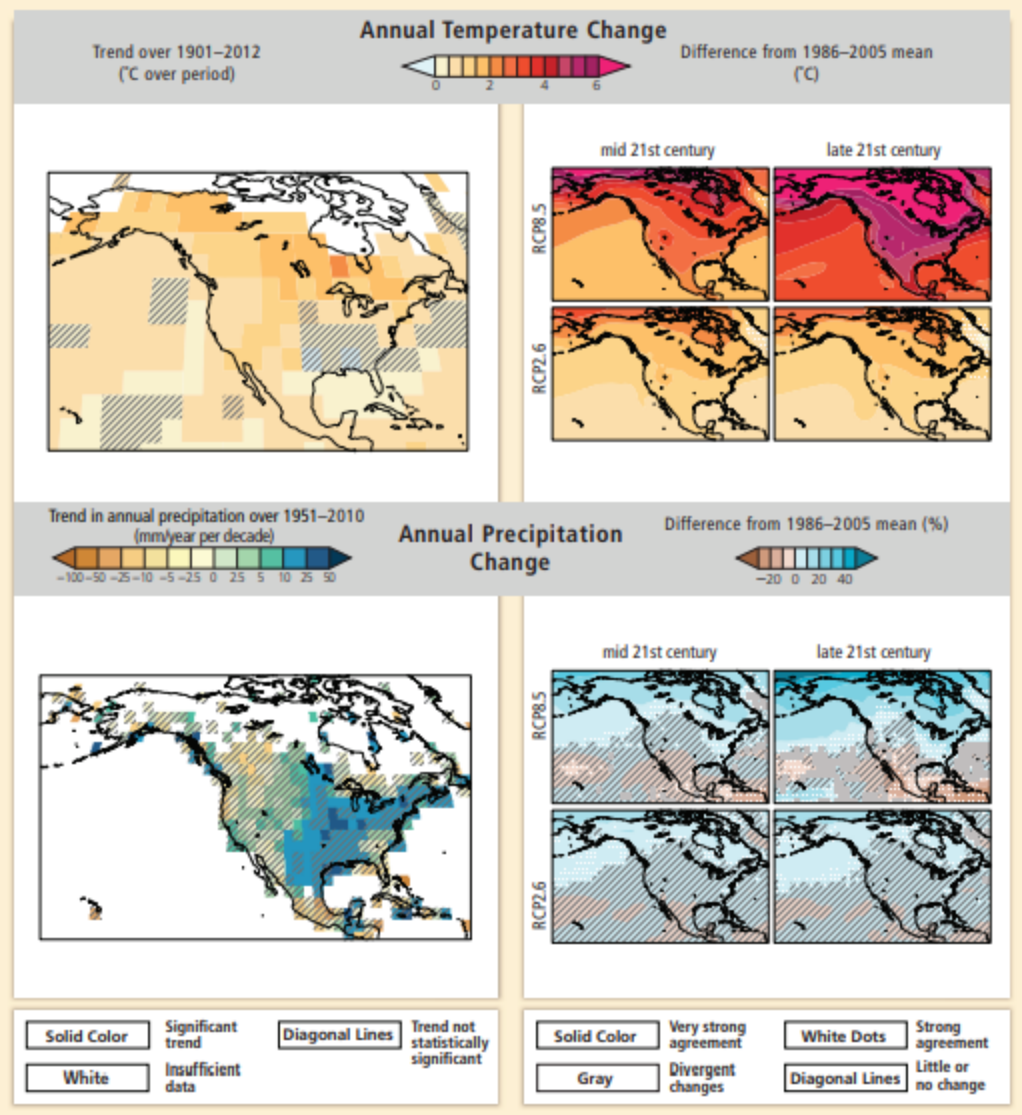

Figure 4. *IPCC projections for temperature and precipitation change in the US (Arias et al. 2021)*

Error in the Data

The outputs carried inherent error due to Landsat 7 imagery. On May 31st, 2003, the scan line corrector (SLC) on the Enhanced Thematic Mapper Plus of Landsat 7 failed, resulting in data gaps in all collected imagery following 2003. Because of this error, I sought to use as little Landsat 7 imagery as possible to limit the influence of error. However, Landsat 7 was the only

active satellite in the Landsat series during the entirety of the 2012 and 2013 growing season. These are the only two years during the study period where Landsat 7 imagery is used.

While the data is still geometrically and radiometrically accurate, it has led to side-effects influencing the imagery visually. One side-effect of the SLC failure is striping, which results in unnatural straight lines in otherwise unaffected images. The red box in Figure 5 highlights striping present in the long-term trend t-test output from GEE. The SLC's influence is present in both the Mann-Kendall and Sen's slope outputs, but it is more noticeable in the Sen's slope image. However, the significant trends data layer appears to be unaffected by the Landsat 7 error, most likely because the two-year range when Landsat 7 imagery was used was outweighed by the over 30 years of correct imagery from Landsats 5 and 8.

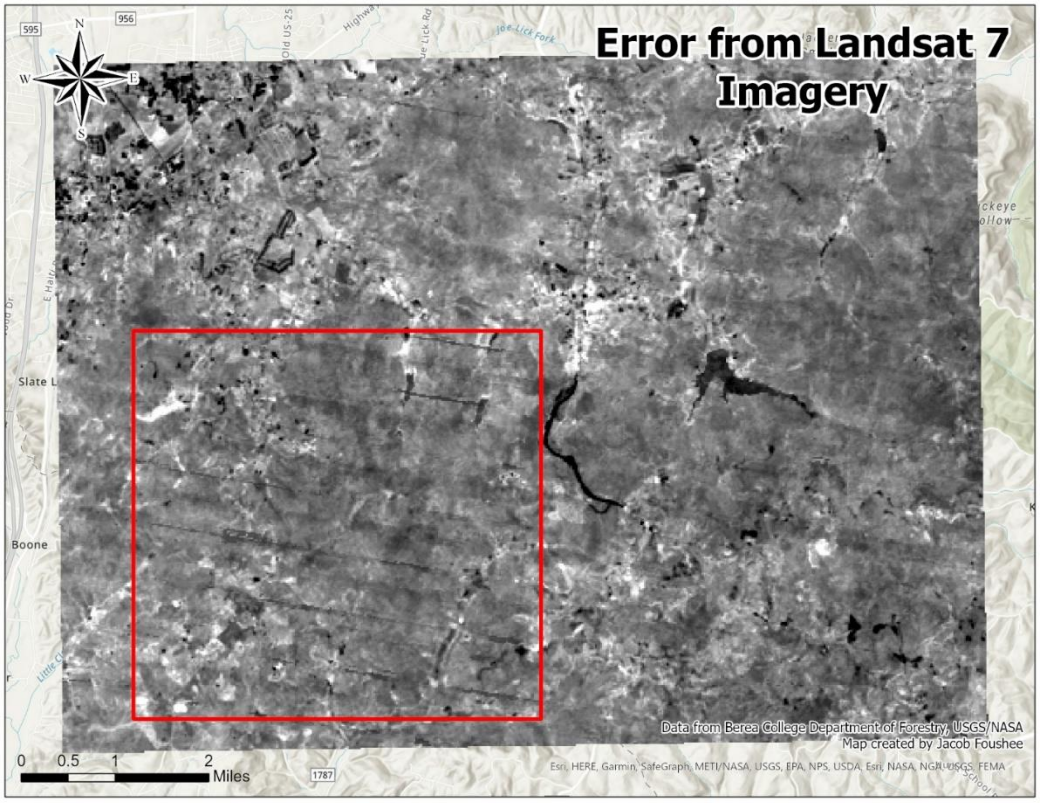

Figure 5. *Data error from Landsat 7 imagery*

CONCLUSION

NDVI is a proxy for photosynthetic activity, and it provides us with a better understanding of the structure of a forest. By studying long-term NDVI trends in forests, researchers can provide foresters data to make informed and effective decisions. In this study, I conducted an analysis of long-term vegetation trends using NDVI. I used Google Earth Engine to evaluate Landsat imagery beginning in 1984 of Berea College Forest (BCF). From this research, I found that 68.47% of all pixels in the study area exhibited significant trends in NDVI, and most of these significant trends were positive. Likewise, I found that NDVI values for the study area increased on average at a rate of 0.001985 units per year. While significant negative trends were present, most of these pixels were clustered around US Highway 241, which was built in 1998. Research into small-scale forests provide researchers a broader base to understand the nuance of vegetation condition at a finer scale. Climate change is expected to continue affecting natural phenology patterns, and further research into factors important in vegetation development can be used to identify these patterns.

REFERENCES

Alencar, A., Shimbo, J. Z., Lenti, F., Marques, C. B., Zimbres, B., Rose, M., Arruda, V., Castro, I., Fernandex Márcico Ribeiro, J. P., Varela, V., Alencar, I., Piontekowski, V., Ribeiro, V., Bustamante, M. M. C., Sano, E. E., and Barroso, M. 2020. Mapping Three Decades of Changes in the Brazilian Savanna Native Vegetation Using Landsat Data Processed in the Google Earth Engine Platform. *Remote Sensing* 12 (6): 924.

Arias, P. A., N. Bellouin, E. Coppola, R. G. Jones, G. Krinner, J. Marotzke, V. Naik, M. D. Palmer, G-K. Plattner, J. Rogelj, M. Rojas, J. Sillmann, T. Storelvmo, P. W. Thorne, B. Trewin, K. Achuta Rao, B. Adhikary, R. P. Allan, K. Armour, G. Bala, R. Barimalala, S. Berger, J. G. Canadell, C. Cassou, A. Cherchi, W. Collins, W. D. Collins, S. L. Connors, S. Corti, F. Cruz, F. J. Dentener, C. Dereczynski, A. Di Luca, A. Diongue Niang, F. J. Doblas-Reyes, A. Dosio, H. Douville, F. Engelbrecht, V. Eyring, E. Fischer, P. Forster, B. Fox-Kemper, J. S. Fuglestvedt, J. C. Fyfe, N. P. Gillett, L. Goldfarb, I. Gorodetskaya, J. M. Gutierrez, R. Hamdi, E. Hawkins, H. T. Hewitt, P. Hope, A. S. Islam, C. Jones, D. S. Kaufman, R. E. Kopp, Y. Kosaka, J. Kossin, S. Krakovska, J-Y. Lee, J. Li, T. Mauritsen, T. K. Maycock, M. Meinshausen, S-K. Min, P. M. S. Monteiro, T. Ngo-Duc, F. Otto, I. Pinto, A. Pirani, K. Raghavan, R. Ranasinghe, A. C. Ruane, L. Ruiz, J-B. Sallée, B. H. Samset, S. Sathyendranath, S. I. Seneviratne, A. A. Sörensson, S. Szopa, I. Takayabu, A-M. Treguier, B. van den Hurk, R. Vautard, K. von Schuckmann, S. Zaehle, X. Zhang, and K. Zickfeld. 2021. Technical Summary. In *Climate Change 2021: The Physical Science Basis. Contribution of Working Group I to the Sixth Assessment Report of the Intergovernmental Panel on Climate Change,* ed. Masson-Delmotte, V., P. Zhai, A. Pirani, S. L. Connors, C. Péan, S. Berger, N. Caud, Y. Chen, L. Goldfarb, M. I. Gomis, M. Huang, K. Leitzell, E. Lonnoy, J.B.R. Matthews, T. K. Maycock, T. Waterfield, O. Yelekçi, R. Yu and B. Zhou, Cambridge University Press. In Press.

Brecht. 2018. Remote Sensing Indices. Available at https://medium.com/regen-network/remote-sensing-indices-389153e3d947 (last accessed 8 October 2021).

Brovelli, M. A., Sun, Y., and Yordanov, V. 2020. Monitoring Forest Change in the Amazon Using Multi-Temporal Remote Sensing Data and Machine Learning Classification on Google Earth Engine. *International Journal of Geo-Information* 9 (10): 580.

Chen, S., Woodcock, C. E., Bullock, E. L., Arévalo, P., Torchinava, P., Peng, S., and Olofsson, P. 2021. Monitoring temperate forest degradation on Google Earth Engine using Landsat time series analysis. *Remote Sensing of Environment* 265: 112648.

Chuine, I., Cour, P., and Rousseau, D. D. 1999. Selecting models to predict the timing of flowering of temperate trees: implications for tree phenology modelling. *Plant, Cell, & Environment* 22 (1): 1-13.

Douglas, E. M, Vogel, R. M., and Kroll, C. N. 2000. Trends in floods and low flows in the United States: impact of spatial correlation. *Journal of Hydrology* 240 (1-2): 90-105.

Dragoni, D. and Rahman, A. F. 2012. Trends in fall phenology across the deciduous forests of the Eastern USA. *Agricultural and Forest Meteorology* 15: 96-105.

Earth Observing System. 2019. Satellite Data: What Spatial Resolution Is Enough?. Available at https://eos.com/blog/satellite-data-what-spatial-resolution-is-enough-for-you/ (last accessed 22 March 2022).

Eastman, J., Sangermano, F., Machado, E. A., Rogan, J., and Anyamba, A. 2013. Global Trends in Seasonality of Normalized Difference Vegetation Index (NDVI), 1982–2011. *Remote Sensing* 5 (10): 4799–4818.

EPA. 2021. Seasonality and Climate Change: A Review of Observed Evidence in the United States. U.S. Environmental Protection Agency, EPA 430-R-21-002. www.epa.gov/climate-indicators/ seasonality-and-climate-change

Forkel, M., Carvalhais, N., Verbesselt, J., Mahecha, M. D., Neigh, C. S. R., and Reichstein, M. 2013. Trend Change Detection in NDVI Time Series: Effects of Inter-Annual Variability and Methodology. *Remote Sensing* 5 (5): 2113–2144.

Gocic, M. and Trajkovic, S. 2013. Analysis of changes in meteorological variables using Mann-Kendall and Sen's slope estimator statistical tests in Serbia. *Global and Planetary Change* 100: 172-182.

Gorelick, N., Hancher, M., Dixon, M., Ilyushchenko, S., Thau, D., and Moore, R. 2017. Google Earth Engine: Planetary-scale geospatial analysis for everyone. *Remote Sensing of Environment* 202: 18-27.

IotaComm. 2020. Licensed Vs. Unlicensed Spectrum: What's The Difference?. Available at https://www.iotacommunications.com/blog/licensed-vs-unlicensed-spectrum/ (last accessed 28 October 2021).

Knipling, E. B. 1970. Physical and physiological basis for the reflectance of visible and near-infrared radiation from vegetation. *Remote Sensing of Environment* 1 (3): 155-159.

Linderholm, H. W. 2006. Growing season changes in the last century. *Agricultural and Forest Meteorology* 137 (1-2): 1-14.

Liu, H. Q. and Huete, A. 1995. A feedback based modification of the NDVI to minimize canopy background and atmospheric noise. *IEEE Transactions on Geoscience and Remote Sensing* 33 (2): 457-465.

Melaas, E. K., Sulla-Menashe, and D., Friedl, M. A. 2018. Multidecadal Changes and Interannual Variation in Springtime Phenology of North American Temperate and Boreal Deciduous Forests. *Geophysical Research Letters* 45 (6): 2679–2687.

Menzel, A. 2000. Trends in phenological phases in Europe between 1951 and 1996. *International Journal of Biometeorology* 44: 76-81.

Naif, S. S., Mahmood, D. A., and Al-Jiboori, M. H. 2020. Seasonal normalized difference vegetation index responses to air temperature and precipitation in Baghdad. *Open Agriculture* 5: 631–637.

Park, S., Jeong, S., Park, Y., Kim, S., Lee, D., M, Y., Jang, D., and Park, K. 2021. Phenological Analysis of Sub-Alpine Forest on Jeju Island, South Korea, Using Data Fusion of Landsat and MODIS Products. *Forests* 12 (3): 286.

Pelkey, N. W., Stoner, C. J., and Caro, T. M. 2000. Vegetation in Tanzania: Assessing long term trends and effects of protection using satellite imagery. *Biological Conservation* 94 (3), 297–309.

Perry, J. T., and Patterson, C, ed. 2000. *A Century of Forestry at Berea College*. Berea College Press.

Piao, S., Liu, Q., Chen, A., Janssens, I. A., Fu, Y., Dai, J., Liu, L., Lian, X., Shen, M., and Zhu, X. 2019. Plant phenology and global climate change: Current progresses and challenges. *Global Change Biology* 25 (6): 1922-1940.

Sankey, T., Belmonte, A., Massey, R., and Leonard, J. 2020. Regional-scale forest restoration effects on ecosystem resiliency to drought: a synthesis of vegetation and moisture trends on Google Earth Engine. *Remote Sensing in Ecology and Conservation* 7 (2): 259-274.

Schmid, J. N. 2017. Using Google Earth Engine for Landsat NDVI time series analysis to indicate the present status of forest stands. B. Sc. Thesis, University of Göttingen.

Tabari, H. and Marofi, S. 2010. Changes of Pan Evaporation in the West of Iran. *Water Resources Management* 25: 97-111.

USDA. 2012. USDA Plant Hardiness Zone Map. Available at https://planthardiness.ars.usda.gov/ (last accessed 28 October 2021)

USGS. 2021a. Landsat Satellite Missions. Available at https://www.usgs.gov/core-science-systems/nli/landsat/landsat-satellite-missions?qt-science_support_page_related_con=0#qt-science_support_page_related_con (last accessed 28 October 2021)

USGS. 2021b. What are the band designations for the Landsat satellites? Available at https://www.usgs.gov/faqs/what-are-band-designations-landsat-satellites?qt-news_science_products=0#qt-news_science_products (last accessed 28 October 2021)

Vitasse, Y., François, C., Delpierre, N., Dufrêne, E., Kremer, A., Chuine, I., and Delzon, S. 2011. Assessing the effects of climate change on the phenology of European temperate trees. *Agricultural and Forest Meteorology* 151 (7): 969-980.

Zhu, Z., Fu, Y., Woodcock, C. E., Olofsson, P., Vogelmann, J. E., Holden, C., Wang, M., Dai, S., and Yu, Y. 2016. Including Land Cover Change in Analysis of Greenness Trends Using All Available Landsat 5, 7, and 8 Images: A Case Study from Guangzhou, China (2000–2014). *Remote Sensing of Environment* 185: 243–257.

APPENDIX

Appendix 1: Source Code

```
var L8 = ee.ImageCollection("LANDSAT/LC08/C02/T1_L2"),
var L7 = ee.ImageCollection("LANDSAT/LE07/C02/T1_L2"),
var L5 = ee.ImageCollection("LANDSAT/LT05/C02/T1_L2"),
var BCF = ee.FeatureCollection("users/fousheejacob/BereaCollegeForest"),
var outputArea =
    ee.Geometry.Polygon(
        [[[-84.31086936558026, 37.59144870864262],
          [-84.31086936558026, 37.4852766025006],
          [-84.1316548880412, 37.4852766025006],
          [-84.1316548880412, 37.59144870864262]]], null, false);

////  NDVI Trend Analysis using Landsat 5, 7, & 8:

////  Study area: Berea College Forest
////  Shapfile imported as "BCF"

//// Load Landsat data to merge and subset so we have no overlaps
//// or duplicates:
L5 = L5.filterDate('1984-01-01', '2011-12-31');
L7 = L7.filterDate('2012-01-01', '2013-12-31');
L8 = L8.filterDate('2014-01-01', '2020-12-31');
//  Merging each image collection into one
var sr = L5.merge(L7).merge(L8);

var years = [1984, 1985, 1986, 1987, 1988, 1989, 1990, 1991, 1992, 1993,
1994, 1995, 1996,
1997, 1998, 1999, 2000, 2001, 2002, 2003, 2004, 2005, 2006, 2007, 2008,
2009, 2010, 2011,
2012, 2013, 2014, 2015, 2016, 2017, 2018, 2019, 2020];
print(years);

var display_min = 0;
var display_max = 100;

//Julian dates of study period
var start_day = 105;  //  Apr 15
var end_day = 288;    //  Oct 15

var cloud_cover = 15;
var cloud_free_percentile = 50;

////  Number of years for each image:
var year_space = 1;

////  Create cloud-free year, day filter and a simple
////  composite using Earth Engine's built-in algorithm:
var quick_LS = function(year){
       var result = ee.ImageCollection(sr)
    .filterDate(ee.Date.fromYMD(year, 1,1), ee.Date.fromYMD(year +
year_space-1, 12,31))
    .filter(ee.Filter.calendarRange(start_day,
end_day)).filterBounds(outputArea);
```

```
  var cfc = result.reduce(ee.Reducer.median()).clip(outputArea);
return cfc;
};

//  Create index with 1/1/year time stamp:
var create_index_w_time_stamp = function(year){
  //  year = ee.Number(year);
        var ls = quick_LS(year);
        var time_start = ee.Date.fromYMD(year, 1, 1).millis();
        var time_end = ee.Date.fromYMD(year + 1, 1, 1).millis();
        if (year >= 2014){
          var NDVI =
ls.normalizedDifference(['SR_B5_median','SR_B4_median']).
setMulti({'system:time_start' : time_start, 'system:time_end' :
time_end});
        } else {
          var NDVI =
ls.normalizedDifference(['SR_B4_median','SR_B3_median']).
setMulti({'system:time_start' : time_start,'system:time_end' : time_end});
        }
        return NDVI;
};

//_____________________________________________________
//  Finalize processing:
//_____________________________________________________


var ndvi_collection =
ee.ImageCollection(years.map(create_index_w_time_stamp));
// print(ndvi_collection);

var trends = ndvi_collection.formaTrend();
var SAMpalette = ['00ff00','008000', '808000', 'ffff00','ffA500',
'ff0000','800000','8c2a04'];
SAMpalette.reverse();

////  Further diagnostics:
// print(trends);

//// M-K Test:
////  As implemented here: https://developers.google.com/earth-
engine/tutorials/community/nonparametric-trends
var afterFilter = ee.Filter.lessThan({
  leftField: 'system:time_start',
  rightField: 'system:time_start'
});

var joined = ee.ImageCollection(ee.Join.saveAll('after').apply({
  primary: ndvi_collection,
  secondary: ndvi_collection,
  condition: afterFilter
```

```
105 }));
106
107 var sign = function(i, j) { // i and j are images
108   return ee.Image(j).neq(ee.Image(i)) // Zero case
109       .multiply(ee.Image(j).subtract(ee.Image(i)).multiply(10000).clamp(-
110 1, 1)).int();
111 };
112
113 var kendall = ee.ImageCollection(joined.map(function(current) {
114   var afterCollection =
115 ee.ImageCollection.fromImages(current.get('after'));
116   return afterCollection.map(function(image) {
117     // The unmask is to prevent accumulation of masked pixels that
118     // result from the undefined case of when either current or image
119     // is masked.  It won't affect the sum, since it's unmasked to zero.
120     return ee.Image(sign(current, image)).unmask(0);
121   });
122   // Set parallelScale to avoid User memory limit exceeded.
123 //}).flatten()).reduce('sum', 2);
124 }).flatten()).reduce('sum').toDouble();
125
126 var palette = ['red', 'white', 'green'];
127 //  Stretch this as necessary.
128 //  Map.addLayer(kendall, { palette: palette, min:-100, max:300 },
129 'kendall');
130 //  Map.addLayer(kendall, {}, 'kendall');
131
132
133 ////  Sen's Slope and Intercept:
134 var slope = function(i, j) { // i and j are images
135   return ee.Image(j).subtract(i)
136       .divide(ee.Image(j).date().difference(ee.Image(i).date(), 'days'))
137       .rename('slope')
138       .float();
139 };
140
141 var slopes = ee.ImageCollection(joined.map(function(current) {
142   var afterCollection =
143 ee.ImageCollection.fromImages(current.get('after'));
144   return afterCollection.map(function(image) {
145       return ee.Image(slope(current, image));
146   });
147 }).flatten());
148
149 var sensSlope = slopes.reduce(ee.Reducer.median(), 2); // Set
150 parallelScale.
151 // Map.addLayer( sensSlope, {palette: palette, min: -0.00001, max: 0.00001
152 }, 'sensSlope');
153 //Map.addLayer(sensSlope, {}, 'sensSlope');
154
155
156 var epochDate = ee.Date('1970-01-01');
```

```
var sensIntercept = ndvi_collection.map(function(image) {
  var epochDays = image.date().difference(epochDate, 'days').float();
  return image.subtract(sensSlope.multiply(epochDays)).float();
}).reduce(ee.Reducer.median(), 2);
// Map.addLayer(sensIntercept, {}, 'sensIntercept');

var sfTimeSeries =
  Chart.image.series(ndvi_collection, outputArea, ee.Reducer.mean(), 200);

////  Binary significance trends
// Values that are in a group (ties).  Set all else to zero.
var groups = ndvi_collection.map(function(i) {
  var matches = ndvi_collection.map(function(j) {
    return i.eq(j); // i and j are images.
  }).sum();
  return i.multiply(matches.gt(1));
});

// Compute tie group sizes in a sequence.  The first group is discarded.
var group = function(array) {
  var length = array.arrayLength(0);
  // Array of indices.  These are 1-indexed.
  var indices = ee.Image([1])
      .arrayRepeat(0, length)
      .arrayAccum(0, ee.Reducer.sum())
      .toArray(1);
  var sorted = array.arraySort();
  var left = sorted.arraySlice(0, 1);
  var right = sorted.arraySlice(0, 0, -1);
  // Indices of the end of runs.
  var mask = left.neq(right)
  // Always keep the last index, the end of the sequence.
      .arrayCat(ee.Image(ee.Array([[1]])), 0);
  var runIndices = indices.arrayMask(mask);
  // Subtract the indices to get run lengths.
  var groupSizes = runIndices.arraySlice(0, 1)
      .subtract(runIndices.arraySlice(0, 0, -1));
  return groupSizes;
};

// See equation 2.6 in Sen (1968).
var factors = function(image) {
  return image.expression('b() * (b() - 1) * (b() * 2 + 5)');
};

var groupSizes = group(groups.toArray());
var groupFactors = factors(groupSizes);
var groupFactorSum = groupFactors.arrayReduce('sum', [0])
      .arrayGet([0, 0]);

var count = joined.count();

```

```
var kendallVariance = factors(count)
    .subtract(groupFactorSum)
    .divide(18)
    .float();
Map.addLayer(kendallVariance, {}, 'kendallVariance', false);


// Compute Z-statistics.
var zero = kendall.multiply(kendall.eq(0));
var pos = kendall.multiply(kendall.gt(0)).subtract(1);
var neg = kendall.multiply(kendall.lt(0)).add(1);

var z = zero
    .add(pos.divide(kendallVariance.sqrt()))
    .add(neg.divide(kendallVariance.sqrt()));
Map.addLayer(z, {min: -2, max: 2}, 'z', false);

// https://en.wikipedia.org/wiki/Error_function#
//Cumulative_distribution_function
function eeCdf(z) {
  return ee.Image(0.5)

.multiply(ee.Image(1).add(ee.Image(z).divide(ee.Image(2).sqrt()).erf()));
}

function invCdf(p) {
  return ee.Image(2).sqrt()
      .multiply(ee.Image(p).multiply(2).subtract(1).erfInv());
}

// Compute P-values.
var p = ee.Image(1).subtract(eeCdf(z.abs()));
Map.addLayer(p, {min: 0, max: 1}, 'p', false);

// Pixels that can have the null hypothesis (there is no trend) rejected.
// Specifically, if the true trend is zero, there would be less than 5%
// chance of randomly obtaining the observed result (that there is a
trend).
var significance = p.lte(0.025);
Map.addLayer(significance, {min: 0, max: 1}, 'significant trends');

////  Visualize time series in the Console:
print(sfTimeSeries, 'LineChart');

////  Zoom to BCF and add shapefile
Map.setCenter(-84.2357424, 37.5394361, 12);

////  Add map layers
Map.addLayer(sensIntercept, {}, 'sensIntercept', false);
Map.addLayer(trends, {bands:'long-trend', min: -0.1, max: 0.1,
palette:SAMpalette},
'Long term trend', false);
```

```
Map.addLayer(ndvi_collection.toBands(), {min: 0, max: 0.7}, 'NDVI
Collection');
Map.addLayer(trends, {bands:'long-tstat', min: -1.68, max: 1.68,
palette:SAMpalette},
'Long term tstat');
Map.addLayer(sensSlope, {palette: palette, min: -0.00001, max: 0.00001 },
'sensSlope');
Map.addLayer(kendall, { palette: palette, min:-100, max:300 }, 'kendall');
Map.addLayer(BCF, {}, 'Berea College Forest');

////  Export data/outputs
// // NDVI_Collection
// Export.image.toDrive({
//   image: ndvi_collection.mean(),
//   description: 'NDVI_Collection',
//   folder: 'Thesis_Output',
//   fileFormat: 'GeoTIFF',
//   crs: 'EPSG:26980',
//   region: outputArea,
//   scale: 30
//   });

// //  Long Term Trend
// Export.image.toDrive({
//   image: trends,
//   description: 'LongTermTrend',
//   folder: 'Thesis_Output',
//   fileFormat: 'GeoTIFF',
//   crs: 'EPSG:26980',
//   region: outputArea,
//   scale: 30
//   });

// // Long Term TStat
// Export.image.toDrive({
//   image: trends,
//   description: 'LongTermTStat',
//   folder: 'Thesis_Output',
//   fileFormat: 'GeoTIFF',
//   crs: 'EPSG:26980',
//   region: outputArea,
//   scale: 30
//   });

// //  Sens Slope
// Export.image.toDrive({
//   image: sensSlope,
//   description: 'SensSlope',
//   folder: 'Thesis_Output',
//   fileFormat: 'GeoTIFF',
//   crs: 'EPSG:26980',
//   region: outputArea,
```

```
//   scale: 30
//   });

// //  Mann-Kendall
// Export.image.toDrive({
//   image: kendall,
//   description: 'Mann-Kendall',
//   folder: 'Thesis_Output',
//   fileFormat: 'GeoTIFF',
//   crs: 'EPSG:26980',
//   region: outputArea,
//   scale: 30
//   });

// //  Sens Intercept
// Export.image.toDrive({
//   image: sensIntercept,
//   description: 'SensIntercept',
//   folder: 'Thesis_Output',
//   fileFormat: 'GeoTIFF',
//   crs: 'EPSG:26980',
//   region: outputArea,
//   scale: 30
//   });

// //  Significance Trend
// Export.image.toDrive({
//   image: significance,
//   description: 'SignificanceTrend',
//   folder: 'Thesis_Output',
//   fileFormat: 'GeoTIFF',
//   crs: 'EPSG:26980',
//   region: outputArea,
//   scale: 30
// });
```